Solid Freeform Fabrication 2023: Proceedings of the 34th Annual International Solid Freeform Fabrication Symposium – An Additive Manufacturing Conference
Reviewed Paper

MULTI-PHYSICS MODELING OF LOW-TEMPERATURE DIRECTED ENERGY DEPOSITION OF STAINLESS STEEL 316L

Kishore MN[*], Dong Qian[*], Wei Li[*]
[*]Department of Mechanical Engineering, The University of Texas at Dallas, TX 75080

Abstract

The Directed energy deposition (DED) process is greatly influenced by the ambient temperature at on-site repair. In Northern Hemisphere locations, DED is particularly influenced by sub-freezing temperatures. However, its influence on the process is not yet studied. This critical gap is fulfilled in this research through a multi-physics computational fluid dynamics (CFD) modeling of the low-temperature DED of the SS316L powders. The model is validated with test cases: $-3°C$ for sub-freezing and $20°C$ for room temperature cases using a cryogenic DED platform. The modeling involves powder spray, local melting, rapid cooling, solidification, evaporation, and fluid-gas interactions. The results show, at sub-freezing, the molten pool is ~63% bigger with the maximum temperature reduced by ~9.5%. The deposition saw an increase in width by ~8.6% and height by ~26% than the room temperature case. Overall, the versatile modeling-experimental platform helps study cryogenic DED cases for in-space additive manufacturing.

Keywords: Directed energy deposition, low temperature, Sub-freezing deposition, Computational fluid dynamics, Multiphysics modeling.

Introduction

Directed Energy Deposition (DED) is a disruptive additive manufacturing (AM) technology wherein a high-power laser heat source is used to melt metallic powders such as stainless steel 316L (SS316L), and others flowing through a coaxial nozzle with the help of inert gas, at the exit of the nozzle [1,2]. The melted powders start depositing directly onto a substrate and layer-by-layer approach to print the metallic components to a required shape and size. The DED process can effectively produce varying sizes and shapes of components made of homogenous metallic alloys, and heterogenous metallic alloys in the form of functional graded materials [3–5]. It can also be used to perform multi-axis printing due to versatile coaxial nozzle arrangements on either CNC platforms or robotic platforms. Recently, metal AM technology has been explored for various applications. One such is the onsite repair applications. When the components are bulk in size, instead of transporting the component onto an AM machine, the AM technology can be moved to the local environment where the bulk component is operating [6–8]. Once the repair location on the component is identified, the repair region in the component can be scanned locally and remapped with the machining, if necessary. After that, AM technology can be used to fill the machined area and bring it to the required shape using post-processing machining. To materialize the true potential of AM technology to the onsite repair application, there needs to be several challenges addressed.

The key to onsite metal repair application is the AM working environment and its influence on the quality of the deposition. Because the metal AM processes like DED have two distinct Multiphysics phenomena compared to traditional manufacturing processes. These are high-power localized heat sources, and rapid cooling of the deposition followed by remelting, and solidification. The quality of the build is directly dependent on the Multiphysics phenomenon.

Under these conditions, how the Multiphysics phenomenon work under different working conditions is yet to be explored. Many researchers have tried to perform AM processes including DED, and wire arc AM (WAAM) at different working conditions. For example, performing DED of steel underwater at room temperature could change the microstructure of the steel [9,10]. The onsite WAAM of the Aluminum underwater and room temperature conditions saw a smaller grain-size microstructure compared to on-air printing. Several researchers so far have effectively used the WAAM process for onsite repair under room temperature conditions [11,12]. Onsite repair through AM reduces supply chain requirements and is environmentally friendly. Deploying AM setups for onsite repair requires AM to perform in remote/austere environments. Deployed in labs for example require AM to perform under controlled regular room temperature conditions [13].

The studies conducted so far use the DED platform for room temperature ~20°C conditions. For onsite repair, the environmental conditions are not room temperature every time and everywhere. For example, in cold regions on Earth such as the northern hemisphere, the temperature is near 0°C or sub-freezing. Further, the temperatures could be below sub-freezing conditions in the cold regions in Space celestial bodies such as Moon or Mars. Hence, there needs to be an effective way to study the DED process for its onsite applications at near or below 0°C. This is specifically a critical study required for in-Space additive manufacturing. Hence, in this research, the effect of the DED process in sub-freezing -3°C in comparison to the room temperature ~20°C is studied using a Multiphysics modeling approach. To study the multiphysical phenomena that are causing phase change, a calibrated computational fluid dynamics (CFD) – volume of fluid (VOF) model is used [14]. Both room temperature and the sub-freezing conditions CFD models are also validated for the geometrical accuracy of the single-track thin wall structures with the cryogenic DED experiments conducted [15].

Computational fluid dynamics modeling of the DED process

The CFD-VOF [16] model consists of a laser heat source model and a coaxial nozzle with a single powder feeder entry point in line with the laser path. The domain as shown in Figure 1 is divided into two regions. The fluid region's top domain is air, and the bottom domain region is the substrate. The deposition happens in the fluid region with air. These two regions have meshed with a grid size of $200\mu m$. The substrate domain size is $1.5"\times0.5" \times 0.25"$. The walls are modeled with symmetric boundary conditions with DED working temperatures, and Z-axis is loaded with atmospheric pressure. Then the full domain is assigned with temperature-dependent fluid and thermal properties. The viscosity of $0.006\ Pa-s$, and the latent heat of fusion of $245\ \frac{kJ}{Kg}$ is kept constant throughout the simulation. The effect of viscosity changes due to temperature was initially assumed to be negligible. Some of these thermofluidic material properties are summarized in Table 1 [17]. The model is solved using a commercially available Flow3D AM CFD solver [18–20].

Table 1: The temperature-dependent material properties of the SS316L considered for the RT-DED and CT-DED case simulation.

Property	270 K	293 K	1000 K	1500 K	2000 K
Thermal Conductivity ($\frac{W}{m-K}$)	12	20	25	32	20
Specific heat ($\frac{J}{Kg-K}$)	420	490	550	680	800
Coefficient of thermal expansion ($\times 10^{-5}$)	1.4	1.5	1.8	2.1	2.1
Density ($\frac{Kg}{m^3}$)	7950	7950	7650	7380	7380

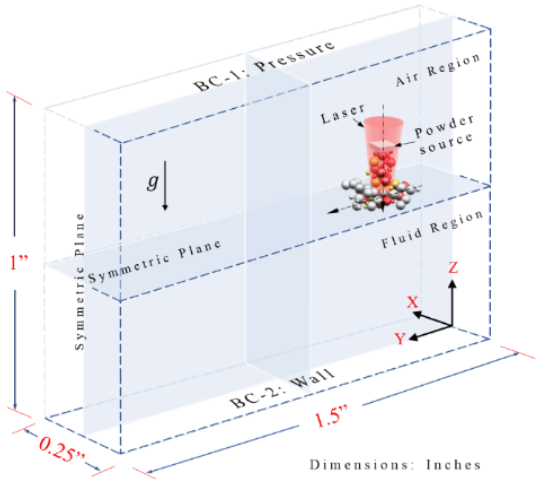

Figure 1: The CFD-VOF model domain considered to simulate the CT-DED and RT-DED case along with its boundary conditions, powder source, laser heat source location, and deposition direction.

In the CFD-VOF model, each grid is assigned a time-dependent fluid fraction step function F to define the fluid state. The function F with a value of 1 represents the state of fluid that exists fully, 0 represents the no-fluid, and in between represents the interface that must contain the free surface. It is governed by partial derivatives in the form of Eq. 1. which is further used to define the boundaries, where $\boldsymbol{v}$ is the velocity vector.

$$\frac{\partial F}{\partial t} + \boldsymbol{\nabla} \cdot (\boldsymbol{v}\ F) = 0 \tag{1}$$

For each cell region, based on the information of F with its dependent variables such as velocities and pressures, conservations of momentum, energy, and mass Eq.2-4.are solved,

$$\frac{\partial \boldsymbol{v}}{\partial t} + (\boldsymbol{v} \cdot \boldsymbol{\nabla})\,\boldsymbol{v} = -\frac{1}{\rho}\ \boldsymbol{\nabla} p + \mu \boldsymbol{\nabla}^2\,\boldsymbol{v} + \boldsymbol{g} + \boldsymbol{f} \tag{2}$$

$$\frac{\partial h}{\partial t} + (\boldsymbol{v} \cdot \boldsymbol{\nabla}) h = -\frac{1}{\rho}\ \boldsymbol{\nabla} \cdot k \boldsymbol{\nabla} T + \dot{q} \tag{3}$$

$$(\boldsymbol{\nabla} \cdot \boldsymbol{v}) = 0 \tag{4}$$

$$\boldsymbol{f} = \left[\sigma \kappa \boldsymbol{n} + \frac{d\sigma}{dT}(\boldsymbol{\nabla} T - \boldsymbol{n}(\boldsymbol{n} \cdot \boldsymbol{\nabla} T))\right] |\boldsymbol{\nabla} F| \frac{2\rho}{\rho_{\boldsymbol{metal}} + \rho_{\boldsymbol{gas}}} \tag{5}$$

where $\boldsymbol{f}$ is the force source representing surface tension force and the Marangoni force at the meltpool zone, given by Eq. 5, where σ is the surface tension, κ is the curvature, $\boldsymbol{n}$ is the surface normal vector, ρ is the volume-averaged density, $\boldsymbol{g}$ is the acceleration due to gravity, μ represents the viscosity, h is the enthalpy, k is the thermal conductivity, and T is the temperature. The Gaussian heat source $\dot{q}$ is given by Eq. 6,

$$\dot{q}(r) = \frac{\eta P_{laser}}{\pi R^2} \exp\left(-\frac{2r^2}{R^2}\right) \tag{6}$$

where P_{laser} is the laser power, R is the laser radius, η is the absorptivity (or absorption rate) of the laser beam that depends on the laser wavelength and the material, and r is the spot radius.
In addition, surface tension phenomena are included in the model to determine the molten pool surface. Except for common effects due to the Marangoni effect and buoyancy effect, the highly concentrated laser energy leads to the evaporation effect at the molten pool surface thereby creating

an additional pressure exerted on the melt pool called recoil pressure. This acts as a major driving force on the molten pool surface and can be calculated by Eq.7, where P_o is the atmospheric pressure, ΔH_v is the enthalpy change, T_v is the evaporation temperature, and R is the universal gas constant.

$$P_r = P_o \exp\left(\frac{\Delta H_v}{R}\left(\frac{1}{T_v} - \frac{1}{T}\right)\right) \tag{7}$$

This evaporation phenomenon involves gaseous/fluid interface, heat transfer, and mass loss. This energy loss due to evaporation is determined by Eq.8, where C_l is the specific heat of the fluid, T_l is the solidus temperature, and L_v is the latent heat of evaporation. The net loss of mass due to evaporation is given by Eq.9, where R_{accom} is the accommodation constant, R is the universal gas constant, M is the molecular weight of the vapor, T is the average liquid temperature at the molten pool, P_v is the vaporization pressure and P_l^{sat} is the saturation pressure.

$$q_{loss} = C_l(T - T_l) + L_v \tag{8}$$

$$M_{net} = R_{accom} * \sqrt{\frac{M}{2\pi R T_{bdy}}} * (P_l^{sat} - P_v) \tag{9}$$

The governing equations to describe the driving force on particle flow in DED are expressed in Eqs. 10-12. Since the initial velocity $\boldsymbol{u}$ of a particle at the powder feeder inlet is a constant value, the particle velocity during the feeding process can be calculated. Therefore, the particle mass distribution during the feeding process will be determined.

$$m_i \frac{d^2\boldsymbol{x}}{dt^2} = \boldsymbol{F_{ij}^c} + \boldsymbol{F_i^f} + \boldsymbol{F_i^g} \tag{10}$$

$$\boldsymbol{F_i^f} = m_i \frac{18\mu}{\rho_p d_p^2} \frac{C_D R_e}{24} \left(\boldsymbol{u} - \boldsymbol{u_p}\right) \tag{11}$$

$$\boldsymbol{F_i^g} = m_i \frac{\boldsymbol{g}\left(\rho_p - \rho\right)}{\rho_p} \tag{12}$$

Eq.10 has the force balance for a particle i, where $\boldsymbol{x}$ denotes the translational displacement of the particle i. $\boldsymbol{F_{ij}^c}$ is the contact force acting on particle i by particle j or the walls. $\boldsymbol{F_i^f}$ is the gas drag force acting on particle i. $\boldsymbol{F_i^g}$ is the gravitational force. In Eq.11, $\boldsymbol{u_p}$, ρ_p, and d_p are the velocity, density, and diameter of the particle, respectively. C_D is the drag coefficient which is a dimensionless quantity. R_e is the Reynolds number and μ is the viscosity of gas flow. In Eq.12, $\boldsymbol{g}$ is the gravitational acceleration.

Further to study the effect of Multiphysics phenomena such as the shapes of the fusion zone, melt pool shape, the effect of heat transfer, and fluid flow and its influence on the deposited structures, the non-dimensional numbers are useful [21]. It helps correlate the processing conditions and their influence on the deposition behavior during and after the deposition sequence. These non-dimensional numbers are the Peclet number, Marangoni number, and Fourier number. Furthermore, the heat input which is the ratio of laser power to scanning speed can be used to compare with the non-dimensional numbers. The non-dimensional heat input is given by Eq.13,

$$Q^* = \frac{PV_{ref}}{VP_{ref}} \tag{13}$$

Where Q^* is the non-dimensional heat input which is dependent on the reference Laser Power P_{ref} and deposition speed V_{ref}, and the chosen Laser Power P and deposition speed V. Similarly, the Peclet number represents the relation between the advection and the diffusion given by Eq.14,

$$Pe = \frac{\rho\, c_p\, v_{max}\, r_s}{k} \tag{14}$$

Where r_s is the radius of the meltpool hemisphere, v_{max} is the maximum velocity in the meltpool zone, and c_p is the specific heat. Further, the influence of surface tension on the fluid flow behavior which affects the size and shape of the deposition is best quantified by the Marangoni number, which is given by Eq.15,

$$Ma = -\frac{d\sigma}{dT}\frac{L_s \Delta T}{\mu\alpha} \tag{15}$$

Where $\frac{d\sigma}{dT}$ is the slope of the surface tension σ and the temperature T (-0.4×10^{-3} N/m-K for SS316L), L_s is the characteristic length of the melt pool zone, ΔT is the temperature difference between solidus and melt pool maximum temperature, μ is the viscosity, and α is the thermal diffusivity ($\alpha = \frac{k}{\rho C_P}$, where k is the thermal conductivity, ρ is the density, and C_P is the specific heat). Similarly, the Fourier number is given by Eq.16,

$$F_o = \frac{\alpha}{V L_s} \tag{16}$$

where V is the scanning speed and L_s is the characteristic length of the melt pool.

Results and Discussion

Cold Temperature DED v/s Room Temperature DED

Meltpool formation and dimensions

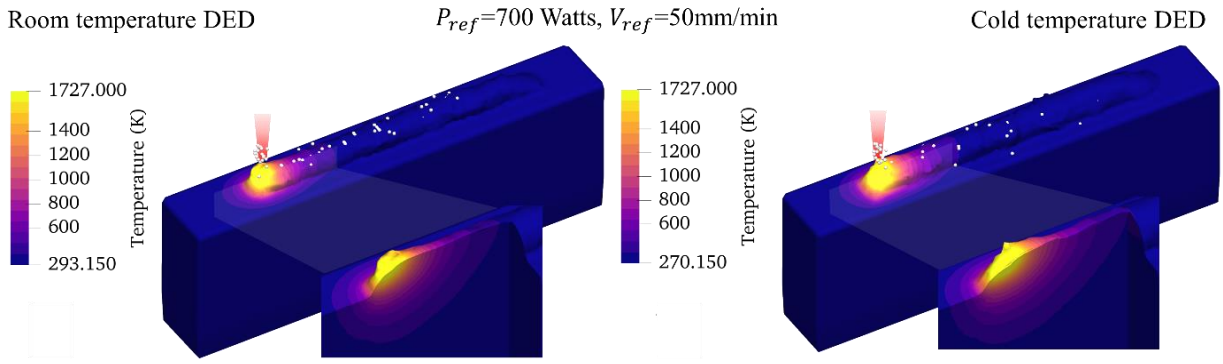

Figure 2: The DED single layer representing the temperature distribution, cross-section heat flow, and thin wall structure. (left) RT-DED full-length deposition view with its temperature distribution against moving laser heat source and powder flow. (right) the CT-DED full-length deposition depicts a bigger deposition compared to RT-DED, with its operating temperature below freezing temperature depicting a wider temperature distribution.

In the simulation methodology, the main goal was set to study the influence of heat transfer and fluid flow on the meltpool formation and the deposition geometry. In the beginning, the reference case was modeled and validated for the geometry of the deposition using a literature experimental source [15]. The CFD-VOF model was calibrated based on the geometry of the deposited single-track single-layer case from the literature source. The reference case considered involves the laser power P_{ref} as 700Watts, and the scanning speed V_{ref} as 50mm/min. these calibrated were further used to simulate different test cases. At first, by keeping the scanning speed constant as V_{Ref}, the heat input was increased through laser power intensity from 1000W to

2500W. Second, by keeping the laser power P_{ref}, the scanning speed was increased from 100mm/min to 400mm/min. The powder feed rate is 4g/min, and the diameter of the particles is 100μm. Each simulation was then investigated for the meltpool formation, deposition geometry, heat flux generated at a cross-section, meltpool zone, solidification phenomenon, thermal diffusion, and heat transfer effects using non-dimensional numbers.

Figure 2 shows the meltpool of the reference case and other simulated cases for RT-DED and CT-DED single track single layer DED cases are shown in Figure 3. The contour is mapped with temperature data as per the data shown in the reference case. In the reference case Figure 2, the deposition in RT-DED and CT-DED cases was normal wherein some heat accumulated near the substrate and transferred to the mushy zone just below the substrate. The meltpool formed slightly bigger in the CT-DED compared to RT-DED. Further, the CT-DED saw higher peak temperatures at the meltpool compared to RT-DED. Figure 3 shows the simulations of RT-DED and CT-DED at four different laser power at reference scanning speeds. The increasing laser power represents the increase in heat input. For RT-DED cases, upon increasing the laser power from 700W to 2000W, there was a formation of the meltpool.

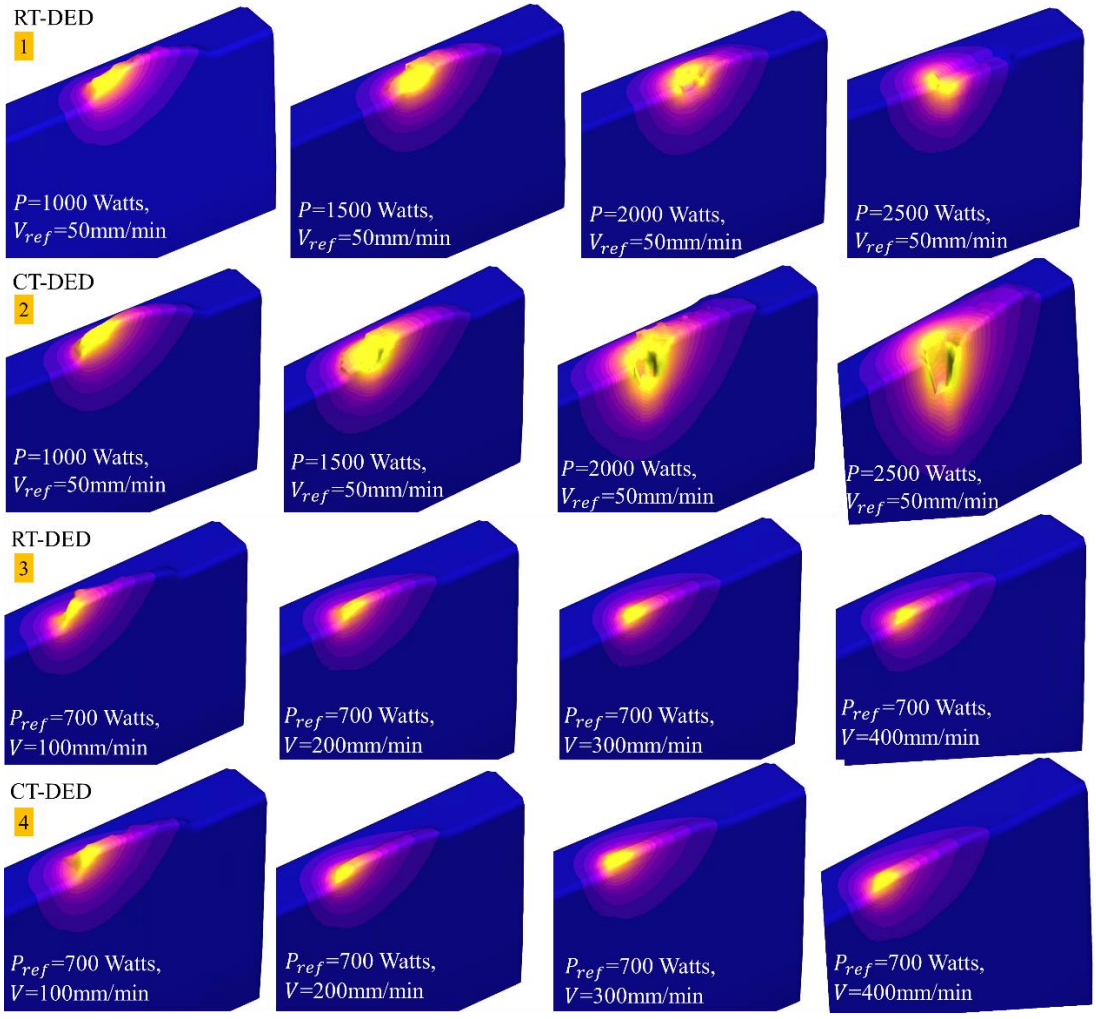

Figure 3: Temperature contours depicted on the single layer RT-DED and CT-DED cases representing the meltpool formation, melt flow, heat affected zone, and deposition. Row 1: RT-DED cases for varying laser power. Row 2: CT-DED cases for varying laser power. Row 3: RT-DED cases for varying scanning speed. Row 4: CT-DED cases for varying scanning speed.

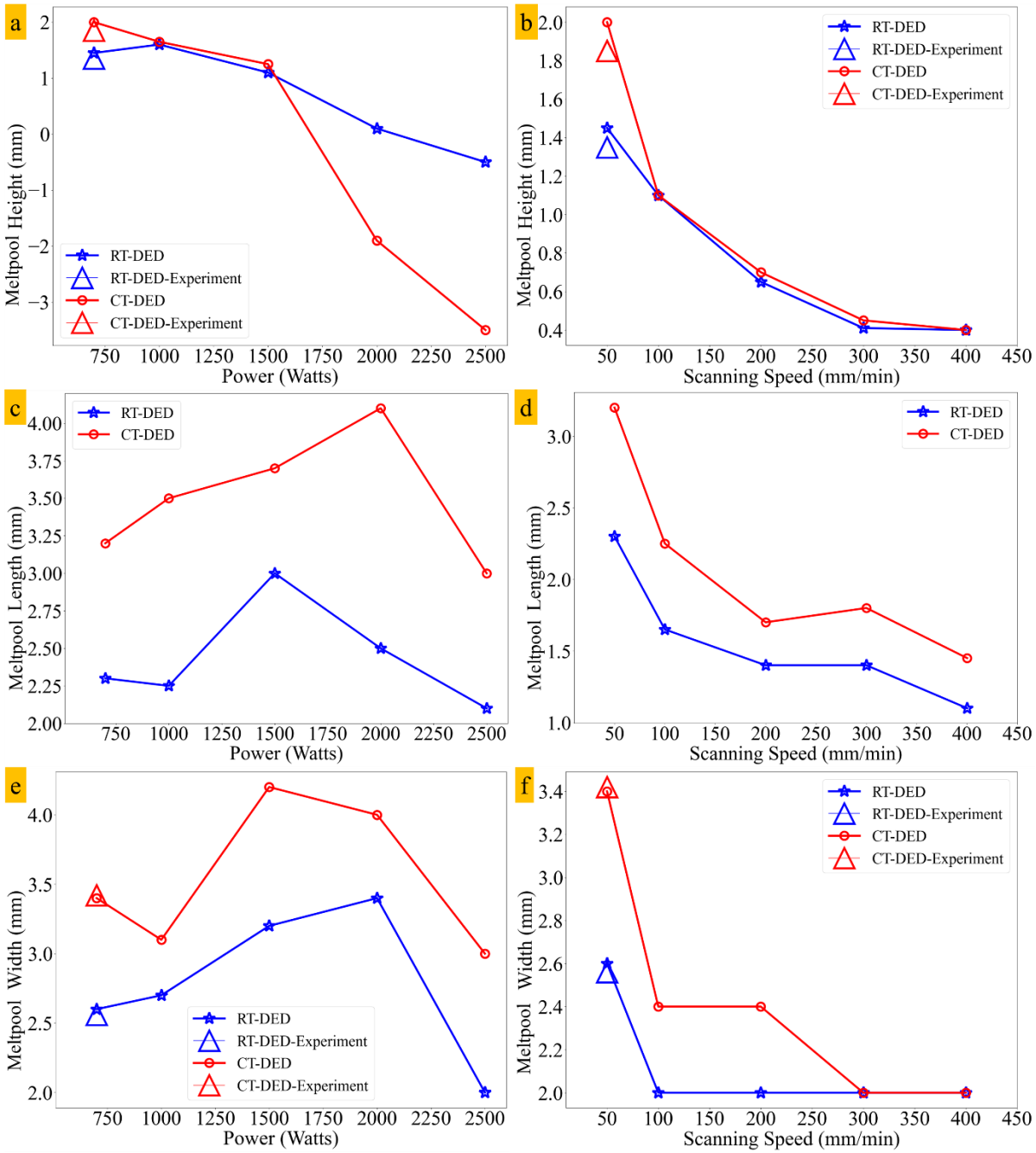

Figure 4: The average meltpool dimensions across the deposition line computed as a function of varying laser power and scanning speed depicting the bigger meltpool dimensions for CT-DED cases. (a) The experimental validation of the height of the meltpool for a reference case and simulated height variation for the varying laser power. (b) simulated height variation for the varying scanning speed. (c) simulated length variation for varying laser power. (d) simulated length variation for varying scanning speeds. (e) The experimental validation of the width of the meltpool for a reference case and simulated width variation for the varying laser power. (f) simulated width variation for the varying scanning speed.

From Figure 3 (Row 1), at power 2500W, the substrate started melting and instead of the metal deposited, there was a ~0.25mm depression across the line of deposition. For the CT-DED case Figure 3 (Row 2), at laser power 1000W and 1500W, the molten pool formation is bigger and wider than the RT-DED case. For power 2000W, even though CT-DED deposition is bigger than the RT-DED case, the molten pool formation changed drastically. The fusion zone saw more substrate melting than all of the RT-DED cases combined. The depression in the fusion zone expanded considerably at the increase of laser power to 2500W. In this power case, there was a meltpool formation until the first 5 seconds, however, it quickly converted to a keyhole formation due to significant substrate melting phenomena. This shows CT-DED can be advantageous to obtain a bigger molten pool at an increase of heat input however, beyond a certain point, it can rapidly turn into keyhole formation.

Contrary to the high heat input cases, keeping the heat input lower at a reference power of 700W, from Figure 3 (Row 3&4), it is observed that at all varying scanning speeds, the CT-DED was an advantage over RT-DED to deposit a bigger molten pool. This also shows, that with minimum heat input, and varying speeds, the CT-DED can deposit a bigger molten pool with higher powder usage efficiency than the RT-DED conditions. To quantify the meltpool dimensions in the simulated cases, the melt pool cross-section height, length, and width were measured, and its average values are compared with varying laser power and scanning speed.

Figure 4 (a-b) shows the height compared with varying laser power and scanning speed. at different time steps, the meltpool dimensions (meltpool length, cross-section width and height) were measured and averaged. It was observed that at P_{ref}, the height of the CT-DED is ~33% higher than the RT-DED. However, the height did not vary for 1000W and 1500W, and both RT-DED and CT-DED heights were mostly similar to the varying speed cases. However, for the high laser power of 2000W and 2500W cases, the height of the CT-DED went negative indicating the negative depth of the fusion zone. This negative fusion zone depth is the keyhole meltpool zone experienced by CT-DED against higher laser power. Compared to the experimental results of measured height, both CT-DED and RT-DED height has an error of <5% for the P_{ref} and V_{ref} case. Further, from Figure 4 (c-d), the CT-DED has an ~45% bigger meltpool in length compared to RT-DED upon varying the power and it is ~23% higher upon varying scanning speed. Similarly, from Figure 4 (e-f), it was observed that the width of the meltpool in the CT-DED case is ~25% wider than the RT-DED case upon varying the laser power. However, upon varying scanning speed, it is ~23% wider only up to 200mm/min. the RT-DED has seen no change in the width after 100mm/min whereas the CT-DED case after 300mm/min was the same as the RT-DED.

Heat transfer in the meltpool zone

To understand the thermal distribution across the cross-section which provides an insight into whether the heat transferred into the substrate or not, the Fourier law of heat conduction was used to analyze the heat flux generated. Looking at the cross-section at t=7 seconds for the laser power cases and at y=1cm for the varying scanning speed cases, the heat flux was calculated based on the peak temperature at the cross-section and the thermal conductivity at the working condition. From Figure 5 (a-b), an interesting characteristic of the CT-DED was observed that irrespective of varying laser power and scanning speed, the heat flux generated at the cross-section by CT-DED was ~60% lesser than the RT-DED. However, since the heat input through laser power was the same for both CT-DED and RT-DED, less heat got conducted across the cross-section in CT-DED compared to RT-DED. This means there is a significant heat accumulated ~50% more than RT-DED in the melt pool fusion zone of the CT-DED cases. This also indicates the conductive mode

of heat transfer is not a dominant mode in CT-DED. However, it also assures that the heat flux generated at the cross-section penetrates through the mushy zone (substrate-deposit interface) which indicates good bonding between the substrate and the deposit. It is to be noted that the thermal conductivity used in the heat flux calculation is assumed to be constant 12W/m-K at T= -3C and 20W/m-K at T=20C.

However, even though heat flux generated at cross-sections ensures good bonding, and conduction mode of heat transfer, it remains steadily low for CT-DED cases of both varying laser power and scanning speed. Thus it does not explain the reason behind the meltpool formation types since the meltpool formation significantly varies for the CT-DED cases at varying laser power cases, and the bigger molten pool dimensions compared to RT-DED cases.

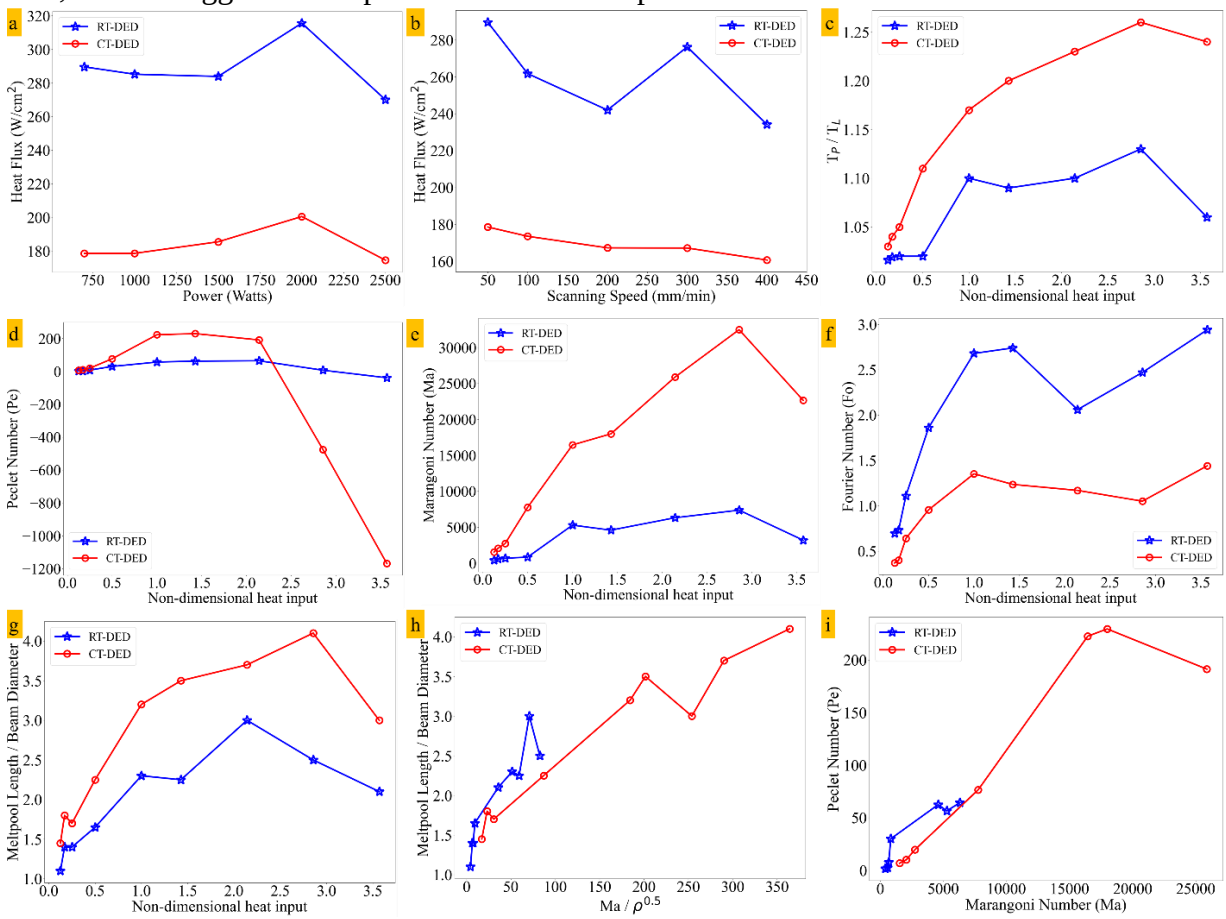

Figure 5: The heat flux, and non-dimensional numbers computed as a function of non-dimensional heat input, varying power, and varying speed depicting the dynamic heat transfer phenomena and meltpool flow patterns in comparison between the CT-DED and the RT-DED. (a) heat flux generated at the cross-section at time t=7 seconds for varying laser power. (b) heat flux generated at the cross-section at deposition location y=1cm from the center of the substrate towards the start of the deposition at varying scanning speeds. (c) the non-dimensional peak temperature to solidus temperature computed as a function of heat input. (d) Peclet number computed as a function of non-dimensional heat input. (e) The Marangoni number is computed as a function of non-dimensional heat input. (f) The Fourier number is computed as a function of non-dimensional heat input. (g) non-dimensional meltpool length against laser beam diameter computed as a function of non-dimensional heat input. (h) non-dimensional meltpool length computed as a function of Ma per $\sqrt{\rho}$. (i) Peclet number computed as a function of Marangoni number.

Another way to look into the heat transfer effect is to analyze the peak temperature between the CT-DED and the RT-DED cases. Since the heat flux generated is directly dependent on the temperature gradient, the peak temperature could provide insights into the effect of varying heat input and the scanning speed. In Figure 5 (c), the variation of the non-dimensional peak temperature as a ratio of peak temperature at the meltpool zone (T_p) and the solidus temperature (T_l) which is material dependent is plotted against the non-dimensional heat input which is dependent on the laser power and the scanning speed. On the abscissa, value 1 represents the reference case, less than value 1 represents the varying speed cases and more than 1 represents the varying laser power cases. For RT-DED, under varying speed cases, the non-dimensional peak temperature was steady at around ~1.02 and ~1.1 steady under varying laser power cases. This means the linear fit slope would remain close to zero. However, for CT-DED, there is a linear trend positive slope for both varying scanning speed and the laser power cases, although with a much greater range of heat inputs with a lesser slope. Hence, in the CT-DED cases, there is a linear trend in the temperature gradient.

Since heat flux generation is directly dependent on the temperature gradient, the CT-DED cases have to accumulate more heat compared to the RT-DED case. However, from the heat flux plots, it was observed that the RT-DED cases saw significantly higher heat flux due to conduction generation compared to CT-DED cases which saw stagnant heat flux generation upon varying laser power and scanning speed. Now analyzing these two aspects together, it can be concluded that, because there is a dominant conductive mode of heat transfer in the RT-DED, there is no variation in the peak temperature ratio for both varying scanning speed and laser power cases. And because there is a lesser dominant conductive heat transfer mode present in the CT-DED, and there exists a higher gradient of the non-dimensional peak temperature, there is significant active heat accumulation happening in the molten pool fusion zone. This heat accumulation could be affecting molten pool size, other heat transfer modes, or fluid flow itself. Put together these aspects, the heat generation and accumulation in the CT-DED cases saw a more dynamic meltpool zone compared to the RT-DED case.

Melt flow patterns

Even though it was understood that CT-DED cases saw significantly higher heat accumulation, the influence of excessive heat accumulation on the melt flow patterns could not be well understood. The shape of the meltpool can change if it is under the influence of the conduction mode of melting, depression mode or keyhole mode of melting. In general, in the conduction mode of melting, the heat energy accumulates over the surface of the substrate, and it exceeds the heat transfer due to conduction. This heat accumulation in the fusion zone raises the meltpool peak temperature to form the meltpool. Similarly, in the keyhole mode of melting, the intensity of the heat energy is very high that the peak temperature in the melt zone reaches the boiling point which will lead to evaporation of the material. This will increase the recoil pressure onto the melt zone which causes the depression which will lead to keyhole modes. Hence, to better understand the melt flow patterns, well-established non-dimensional numbers such as the Peclet number, Marangoni number, and Fourier number were used.

Figure 5 (g) shows the variations in the non-dimensional meltpool length to the laser beam size of 1mm adopted in the simulation as a function of non-dimensional heat input. The results show the meltpool lengths are the highest for the CT-DED compared to RT-DED irrespective of varying power or the scanning speed. Higher heat input has increased the meltpool length significantly for the CT-DED cases. Figure 5 (d) shows the Peclet number computed as a function

of the non-dimensional heat input. For the varying scanning speed cases, the Peclet number did not change much between the CT-DED and the RT-DED cases, whereas for the varying laser power cases, the Peclet number was positive up to 1500W for CT-DED, and 2000W for RT-DED. Further, up to 1500W, the Pe was higher for CT-DED compared to RT-DED. This means, under CT-DED conditions, the mass flow rate due to the convective mode is higher than the thermal diffusion. The convective mass transfer here is dependent on the flow velocity and the characteristic length which is the molten pool height. It was noticed before that up to 1500W, the height distribution between CT-DED and RT-DED did not see many variations except for ~30% variation in the reference case. This means, under CT-DED conditions, the flow velocity is significantly higher than the RT-DED conditions. This flow effect helps spread the meltpool both longitudinally and transversely up to 1500W for CT-DED.

Furthermore, from 2000W onwards, for CT-DED cases, it was observed that both flow velocity and characteristic length considering the depression are substantially higher than RT-DED. It was noted before that heat flux generation due to conduction remains steady and low in these cases. This means, under these laser power conditions, the peak temperature in the meltpool zone is reaching the boiling point, and higher flow velocity is causing higher convective mass transfer. The excessive heat accumulation in these CT-DED cases is pushing the peak temperature to reach boiling point causing an evaporation effect leading to higher recoil pressure exerting on the meltpool zone from the opposite direction. This high recoil pressure and higher convective mass transfer reverse the flow direction. This reverse flow direction can be observed through the negative Peclet number. Hence, instead of depositing, there was a depression with greater depth.

Figure 5 (e) represents the Marangoni number computed as a function of non-dimensional heat input. for CT-DED cases, under varying scanning speed, Ma range between 1500-8000 linearly, and for RT-DED, this is ranging between 400-850. Under varying laser power conditions, CT-DED saw a greater range of Ma between 16000-33000. For RT-DED, this was 5000-7500. The greater Ma for CT-DED compared to RT-DED again reflects higher liquid metal velocities in the melt pool zone. It highlights a higher convective heat transfer within the molten pool. To understand the influence of convective heat transfer in the melt zone and dimensions, the effect of density could be minimized since the density in the simulation model is not varying drastically. Hence, analyzing the results as a combined effect of density and Ma is computed against the non-dimensional meltpool length and laser beam diameter. From Figure 5 (h) was observed that, given the volume, CT-DED has a greater length ratio of the molten pool compared to RT-DED for high heat input cases. CT-DED also has a greater convective heat transfer within the molten pool. It was also observed that the varying speed cases of CT-DED cases match closely with the varying laser power of RT-DED since the CT-DED's Ma falls within the range of RT-DED. As noted in the Figure 5 (i), an increase in Ma also results in higher values of Pe. The CT-DED higher laser power cases has a greater slope compared to all the cases of the RT-DED. Further, CT-DED varying scanning speed cases also exhibit a linear increase in the Pe/Ma ratio compared to a lesser cluster value for RT-DED cases. Together, the higher Pe and Ma explains the advantages of CT-DED given the varying heat input and the scanning speed, it exhibits higher aspect ratio of the molten pool.

Finally, to understand the effect of thermal diffusion in the molten pool, a non-dimensional Fourier number was used and computed as a function of non-dimensional heat input. From Figure 5 (f), it was observed that the thermal diffusion is exceedingly higher for the RT-DED cases compared to CT-DED cases and has the same trend for both varying laser power and scanning speed. Under varying scanning speed conditions, the Fo for CT-DED has a range 0.35-0.95

whereas for RT-DED this is 0.7-1.9. This means the thermal diffusivity for RT-DED is almost double that of CT-DED for varying scanning speed conditions. Further, under varying laser power conditions, the Fo for RT-DED varies between 1.8-3.0, whereas for CT-DED, it varies between 0.9-1.4. Here also, the thermal diffusivity is almost double for RT-DED compared to CT-DED. This means, for CT-DED, there is a high heat accumulation as a result of low thermal diffusivity.

Conclusion

In this study, the DED process was used to print SS316L powder at different cold ambient temperatures (20°C and -3°C). The experimental findings helped calibrate the model to depict the onsite DED process near freezing point temperature. It was found that at cold ambient temperatures, the DED process can be carried out smoothly. Furthermore, the molten pool was easily formed; and lowering the ambient temperature increases the molten pool size. At the cold ambient temperature in this study (-3°C), the sample had the largest molten pool size and largest cross-section height. To further understand the Multiphysics of the CT-DED, keeping the reference case of 700W laser power and the 50mm/min scanning speed, different simulations were carried out at varying laser power from 700W – 2500W at V_{ref} of 50mm/min, and varying scanning speed from 50mm/min – 400mm/min at P_{ref} of 700W.

At first, during reference case, varying laser power and scanning speed cases, the CT-DED exhibited meltpool formation of either conductive mode, convective mode, or depression or keyhole mode of melt pattern. In comparison, CT-DED at varying laser power, up to 1500W has exhibited a larger molten pool under a less dominant conductive mode and dominant convective mode of heat transfer. Increasing the laser power from 2000W, the CT-DED, due to high convective mode, and greater melt flow, exhibited a keyhole mode of meltpool formation pattern. Further, the CT-DED meltpool dimensions across the varying laser power and scanning speed are significantly higher than the RT-DED. The cumulative length of the meltpool is ~65% greater than the RT-DED for high laser power cases and is ~60% greater than the RT-DED for varying scanning speed cases. A similar trend was observed for the width dimension. However, for the height, except for the reference case, CT-DED was ~5%-20% greater than the RT-DED. This excludes the special cases wherein the keyhole mode of melt flow pattern was observed at varying laser power beyond 2000W.

Second, there is a dominant conductive mode of heat transfer in the RT-DED, and also there is no variation in the peak temperature ratio for both varying scanning speed and laser power cases in RT-DED cases. For CT-DED, there is a lesser dominant conductive heat transfer mode present, and there exists a higher gradient of the non-dimensional peak temperature, thereby indicating a significantly active heat accumulation happening in the molten pool fusion zone. From non-dimensional numbers, it was observed that the excessive heat accumulation in these CT-DED cases affected the peak temperature to reach boiling point causing an evaporation effect leading to a higher recoil pressure exerted on the meltpool zone from the opposite direction. This high recoil pressure and higher convective mass transfer reverses the flow direction causing meltpool instead of depositing, a depression with greater depth was developed.

Third, for the CT-DED cases, the high Pe and Ma represent a dominant convective mode of mass transfer compared to RT-DED. From lower Fo, it can be concluded that for CT-DED, the thermal diffusion phenomena are occurring at a much slower pace which on the contrary a very rapid pace for the RT-DED cases. This means the CT-DED cases will exhibit a bigger molten pool compared to RT-DED cases due to less thermal diffusion, more heat accumulation in the meltpool

zone, less dominant conductive mode of heat transfer, and greater dominant convective mode of mass transfer. However, beyond certain heat input as in this case 2000W, the dominant convective mode and excessive heat accumulation will turn a negative impact in the melt zone causing greater recoil pressure. This greater recoil pressure together with lower thermal diffusion will immediately cause the melt flow pattern to turn into depression mode causing keyhole effects.

Overall, the CT-DED cases have shown greater meltpool dimensions compared to RT-DED. The CT-DED cases depicted an advantageous process and method for on-site repair applications wherein under the influence of lower heat input and/otherwise up to critical heat inputs, and for varying speeds, the molten pool is bigger than the RT-DED cases. The multiphysical modeling calibrated with the experimental observations on the geometry of the meltpool and deposition has demonstrated modelling capabilities in identifying key reasons for the drastic changes in the meltpool dimensions, meltpool formations, melt flow patterns, and heat transfer phenomena between the room temperature and cold temperature directed energy deposition process for stainless steel 316L.

Credit authorship contribution statement

Kishore MN: Conceptualization, methodology, formal analysis, investigation, data curation, writing, visualization.
Dong Qian: Resources, supervision, project administration.
Wei Li: Resources, supervision, project administration, experimental validation.

Declaration of competing interests

The authors declare that they have no known competing financial interests or personal relationships that could have appeared to influence the work reported in this paper.

Data availability

The raw/processed data required to reproduce these findings can be provided upon request.

References

[1] G. Piscopo, L. Iuliano, Current research and industrial application of laser powder directed energy deposition, International Journal of Advanced Manufacturing Technology. 119 (2022) 6893–6917. https://doi.org/10.1007/s00170-021-08596-w.

[2] M. Lalegani Dezaki, A. Serjouei, A. Zolfagharian, M. Fotouhi, M. Moradi, M.K.A. Ariffin, M. Bodaghi, A review on additive/subtractive hybrid manufacturing of directed energy deposition (DED) process, Advanced Powder Materials. 1 (2022) 100054. https://doi.org/10.1016/j.apmate.2022.100054.

[3] W. Li, J. Zhang, X. Zhang, F. Liou, Effect of optimizing particle size on directed energy deposition of Functionally Graded Material with blown Pre-Mixed Multi-Powder, Manuf Lett. 13 (2017) 39–43. https://doi.org/10.1016/j.mfglet.2017.07.001.

[4] W. Li, L. Yan, X. Chen, J. Zhang, X. Zhang, F. Liou, Directed energy depositing a new Fe-Cr-Ni alloy with gradually changing composition with elemental powder mixes and particle size' effect in fabrication process, J Mater Process Technol. 255 (2018) 96–104. https://doi.org/10.1016/j.jmatprotec.2017.12.010.

[5] W. Li, M.N. Kishore, R. Zhang, N. Bian, H. Lu, Y. Li, D. Qian, X. Zhang, Comprehensive studies of SS316L/IN718 functionally gradient material fabricated with directed energy deposition: Multi-physics & multi-materials modelling and experimental validation, Addit Manuf. 61 (2023). https://doi.org/10.1016/j.addma.2022.103358.
[6] R. Zhang, K.M. Nagaraja, N. Bian, E. Fisher, S. Ahmadyar, K. Bayazitoglu, H. Lu, W. Li, Experimental studies on fabricating functionally gradient material of stainless steel 316L-Inconel 718 through hybrid manufacturing: directed energy deposition and machining, International Journal of Advanced Manufacturing Technology. 120 (2022) 7815–7826. https://doi.org/10.1007/s00170-022-09304-y.
[7] A. Dass, A. Moridi, State of the art in directed energy deposition: From additive manufacturing to materials design, Coatings. 9 (2019). https://doi.org/10.3390/COATINGS9070418.
[8] A. Shrivastava, S. Anand Kumar, S. Rao, B.K. Nagesha, S. Barad, T.N. Suresh, Remanufacturing of nickel-based aero-engine components using metal additive manufacturing technology, in: Mater Today Proc, Elsevier Ltd, 2021: pp. 4893–4897. https://doi.org/10.1016/j.matpr.2021.01.355.
[9] Z.D. Wang, G.F. Sun, M.Z. Chen, Y. Lu, S.B. Zhang, H.F. Lan, K.D. Bi, Z.H. Ni, Investigation of the underwater laser directed energy deposition technique for the on-site repair of HSLA-100 steel with excellent performance, Addit Manuf. 39 (2021). https://doi.org/10.1016/j.addma.2021.101884.
[10] V. Thampy, A.Y. Fong, N.P. Calta, J. Wang, A.A. Martin, P.J. Depond, A.M. Kiss, G. Guss, Q. Xing, R.T. Ott, A. van Buuren, M.F. Toney, J.N. Weker, M.J. Kramer, M.J. Matthews, C.J. Tassone, K.H. Stone, Subsurface Cooling Rates and Microstructural Response during Laser Based Metal Additive Manufacturing, Sci Rep. 10 (2020). https://doi.org/10.1038/s41598-020-58598-z.
[11] C. Liu, N. Guo, Q. Cheng, Y. Fu, X. Zhang, In situ formation of laser-cladded layer on thin-walled tube of aluminum alloy in underwater environment, Materials. 14 (2021). https://doi.org/10.3390/ma14164729.
[12] Z. Liu, Q. Jiang, W. Cong, T. Li, H.C. Zhang, Comparative study for environmental performances of traditional manufacturing and directed energy deposition processes, International Journal of Environmental Science and Technology. 15 (2018) 2273–2282. https://doi.org/10.1007/s13762-017-1622-6.
[13] R. Zhang, N. Bian, H. Lu, Y. Li, Y. Tian, W. Li, Molten pool swing in printing the steel/inconel functionally gradient material with laser-based Directed Energy Deposition, Manuf Lett. 32 (2022) 44–48. https://doi.org/10.1016/j.mfglet.2022.03.002.
[14] H.L. Wei, T. Mukherjee, W. Zhang, J.S. Zuback, G.L. Knapp, A. De, T. DebRoy, Mechanistic models for additive manufacturing of metallic components, Prog Mater Sci. 116 (2021). https://doi.org/10.1016/j.pmatsci.2020.100703.
[15] W. Li, R. Zhang, M.N. Kishore, Y. Jiao, N. Bian, H. Lu, D. Qian, X. Zhang, S. Karnati, Experimental Study of Low-Temperature Directed Energy Deposition Near Freezing Point Temperature 0°C, JOM. (2023). https://doi.org/10.1007/s11837-023-05958-5.
[16] C.W. Hirt, B.D. Nichols, Volume of Fluid (VOF) Method for the Dynamics of Free Boundaries*, 1981.
[17] K.C. Mills, Recommended values of thermophysical properties for selected commercial alloys, Woodhead Publishing Ltd, Cambridge, England, 2002.

[18] K.M. Nagaraja, W. Li, D. Qian, V. Vasudevan, Y. Pyun, H. Lu, Multiphysics modeling of in situ integration of directed energy deposition with ultrasonic nanocrystal surface modification, International Journal of Advanced Manufacturing Technology. 120 (2022) 5299–5310. https://doi.org/10.1007/s00170-022-09082-7.
[19] R. Mathews, K.M. Nagaraja, R. Zhang, S. Sunny, H. Yu, D. Marais, A. Venter, W. Li, H. Lu, A. Malik, Temporally continuous thermofluidic–thermomechanical modeling framework for metal additive manufacturing, Int J Mech Sci. 254 (2023). https://doi.org/10.1016/j.ijmecsci.2023.108424.
[20] Flow Science.Inc, FLOW-3D 2022 R1, (n.d.). https://www.flow3d.com/products/flow-3d/flow-3d-2022r1/ (accessed March 7, 2022).
[21] T. Mukherjee, V. Manvatkar, A. De, T. DebRoy, Dimensionless numbers in additive manufacturing, J Appl Phys. 121 (2017). https://doi.org/10.1063/1.4976006.